Phase diagrams and thermodynamics of core materials

Andrew Campbell

Department of the Geophysical Sciences, University of Chicago

Accepted August 19, 2015 for AGU Monograph:

Deep Earth: Physics and Chemistry of the Lower Mantle and Core

Abstract

The density contrast at Earth's inner core boundary can act as an important constraint on the chemical and thermal structure of the core, if the melting relationships of relevant Fe-rich alloys were accurately known. Currently, there are no experimental constraints on these solid–melt phase loops at appropriately high pressure, temperature conditions. However, a simplified thermodynamic analysis, using available melting curves for Fe-rich binaries and their endmember alloys, suggests that high pressure melting relations can be reasonably approximated using an entropy change of melting of ΔS_m = 0.70-0.75 R for these systems. With this parameter, and extrapolated melting curves, multicomponent phase diagrams are calculated to inner core boundary conditions. The phase relations so calculated are compatible with geophysical constraints on the alloy in Earth's core.

Introduction

The differentiation of the Earth into its metallic core and rocky mantle and crust is one of the most significant events in the planet's formation and evolution. The composition and dynamics of the core today carry the imprint of those early differentiation processes, and a closer understanding of the core's current composition and thermal state would provide insight into the chemical and physical conditions relevant to the birth of our planet. Cosmochemical abundances and the seismological structure of Earth's deep interior together indicate that the core's main constituent is iron, alloyed with ~5 wt% nickel and perhaps ~10 wt% of lighter elements [Birch, 1952]. This light element alloying component is regarded to be mainly S, O, Si, and/or C, in uncertain relative importance, and other elements including H and Mg are also sometimes considered potentially important. An important research goal in high pressure mineral physics is to better define the light element component of Earth's core, whose identity will improve our understanding of Earth's formation and current thermal structure.

Mineral physics investigations into the core's light element component rest on the comparison between measured or computed properties of a candidate alloy with the seismologically determined density and velocity structure of the core, which provide several key constraints. First, the density and velocity of the outer core must be satisfied by the properties of the alloy. This is an important and widely used constraint, but ultimately limited because the tradeoffs between compositions and temperature leave the problem underdetermined. An important additional constraint is the density (and velocity) jump at the inner core boundary (ICB), which is a consequence of crystallization of a denser solid inner core from the liquid, light element-rich outer core. This 7% density contrast [*Masters and Gubbins*, 2003] represents a compositional tie

line in the phase relations that describe the properties of the core's alloy composition at the ICB pressure (330 GPa) and temperature (uncertain, but in the range of 5000 K). A successful candidate core composition will match this solid/liquid density contrast on its liquidus at the ICB temperature, and moreover, an adiabat for the model composition anchored near that ICB temperature defines, through the alloy's equation of state, the density and velocity profiles that must match those of PREM [*Dziewonski and Anderson*, 1981] or any similar seismological model for the core.

There has been considerable progress defining the equations of state and velocities for various iron alloy compositions at high pressures and temperatures. A combination of static and dynamic experimental studies, as well as ab initio investigations, have provided a useful set of equations of state constrained to core pressures for Fe [e.g. *Dewaele et al.,* 2006], FeO [e.g. *Jeanloz and Ahrens*, 1980; *Campbell et al.*, 2009; *Fischer et al.*, 2011], FeS and Fe_3S [e.g. *Brown et al.*, 1984; *Seagle et al.,* 2006; *Fei et al.,* 2000; *Kamada et al.*, 2014b], Fe_3C [*Sata et al.,* 2010; *Litasov et al.*, 2013], and Fe–Si alloys [*Fischer et al.*, 2012; 2014]. In addition, velocity data are available for many iron-rich alloys to high pressures based on inelastic X-ray scattering measurements [e.g. *Badro et al.,* 2007; *Antonangeli et al.*, 2010; *Mao et al.*, 2012; *Kamada et al.*, 2014a; *Chen et al.*, 2014]. Improvement in this direction is still needed, of course—particularly in obtaining data from appropriate liquid alloys [*Morard et al.,* 2013], and higher experimental P, T conditions covering the entire range of Earth's core—but the available data are adequate to resolve density and velocity comparisons to the core.

In contrast, the phase diagrams of candidate core-forming alloys are much more poorly resolved,

and this is nonetheless the subject of the present chapter. The tools that have permitted impressive growth in our understanding of the physical properties of iron-rich alloys—namely synchrotron X-ray scattering methods in diamond anvil cells, and dynamic compression studies—are not as well suited for detailed chemical investigations. Prospects for the near future are good though, because improvements in sample recovery methods (principally focused ion beam micromachining) promise to allow petrological studies of these and other geologically relevant systems to core conditions. Recent studies have reported high resolution electron microscopy of samples recovered from outer core conditions [e.g. *Nomura et al.*, 2014], and one can anticipate that similar studies on candidate core compositions will soon follow. In the meantime, however, there is lamentably poor understanding of Fe-rich phase diagrams at the *P*, *T*, *X* conditions relevant to Earth's inner core boundary. There is no experimental information on solid/melt partitioning in Fe-alloys at the conditions of Earth's core, much less at the more extreme conditions of the ICB. Consequently there are no data with which to benchmark the accuracy of the handful of ab initio studies that exist on this subject [e.g. *Alfè et al.*, 2007; *Zhang and Yin*, 2012]. In this chapter I review the essential thermodynamics of the melting relations in core-forming alloys and apply these principles to the limited available data, in hope of outlining where future experimental studies can best be applied to constrain the composition of Earth's core.

Thermodynamic Basis

Here we consider the thermodynamics of phase loops during eutectic melting of Fe-rich alloys relevant to studies of Earth's core. The binary alloy endmembers (FeO, FeSi, Fe_3S, and Fe_3C) are described here using an associated solution model, applied previously for this use by *Stevenson* [1981] and *Svendsen et al.* [1989]. In associated Fe–Z solutions, the solute Z is present as

monomers in addition to associated Fe_iZ_j complexes [*Prigogine and Defay*, 1954]. Although binary compounds are sometimes taken as the solute (e.g. FeO in *Komabayashi* [2014]), associated solution models successfully describe both alloy solutions (e.g. *Sharma and Chang*, 1979; *Chuang and Chang*, 1982) and silicate melts [*Wen and Nekvasil*, 1994; *Ghiorso*, 2004]. The purpose of revisiting this approach is that there is now more detailed information available for not only the melting curves of some endmembers but also the binary eutectics between them. This information can be used, in the context of the associated solution model, to estimate the shapes of the liquidus curves, including the eutectic compositions. Furthermore, we extend this model here to multicomponent Fe-rich alloy systems, whereas the earlier analyses were restricted to binary systems because of the limited experimental data available.

For endmember compositions the chemical potential of the liquid (μ_0^L) can be related to that of the solid (μ_0^S) to first order by

$$\mu_0^L = \mu_0^S - \Delta S_m (T - T_m) \quad (1)$$

where ΔS_m is the entropy change upon melting and T_m is the melting temperature of the pure substance. Here, differences in heat capacity between solid and liquid are assumed negligible near the melting point. Accordingly, in a solid–liquid phase loop the activities (a) of this endmember component are related to one another by

$$\ln \frac{a^L}{a^S} = \frac{\Delta S_m}{RT}(T - T_m) \quad (2)$$

because $\mu_i^L = \mu_i^S$ for each component i in the solutions, and $\mu = \mu_0 + RT \ln a$. This approach was

used, for example, by *Williams and Jeanloz* [1990] to estimate the eutectic from melting curves of Fe and FeS, assuming a value for ΔS_m. Below we will build upon recent measurements of eutectic temperatures to evaluate ΔS_m at high pressures for different binary systems, allowing us to extend the existing data to inner core boundary conditions with greater confidence in our assumptions.

For binary compounds Fe_iZ_j, where Z represents any candidate light element in the core, we model both the solid and liquid phases as fully associated mixtures, such that FeO, Fe_3S, etc. are distinct, energetically favored species in both phases: i Fe + j Z $\leftrightarrow$ Fe_iZ_j. This leads to [*Prigogine and Defay*, 1954]:

$$(3) \qquad \begin{aligned} \mu_{Fe_iZ_j} &= i\mu_{Fe} + j\mu_Z = i\mu_{0,Fe} + iRT\ln a_{Fe} + j\mu_{0,Z} + jRT\ln a_Z \\ &= \mu_{0,Fe_iZ_j} + RT\ln a_{Fe_iZ_j} \end{aligned}$$

where μ_0 for Fe_iZ_j refers to the stoichiometric endmember, with mole fraction $X_Z = j/(i+j)$. From (3),

$$(4) \qquad a_{Fe_iZ_j} = a_{Fe}^i a_Z^j e^{-\Delta\mu/RT}$$

with the definition $\Delta\mu = \mu_{0,FeiZj} - i\,\mu_{0,Fe} - j\,\mu_{0,Z}$. This term can be obtained by considering that $a_{FeiZj} = 1$ at $X_{Fe} = i/(i+j)$, $X_Z = j/(i+j)$. Assuming ideal solution behavior for each element, $e^{-\Delta\mu/RT} = (i+j)^{i+j} / (i^i j^j)$ and (4) becomes

$$(5) \qquad a_{Fe_iZ_j} = \frac{(i+j)^{i+j}}{i^i\, j^j} X_{Fe}^i X_Z^j$$

Equations (2) and (5) describe the phase relations between liquid and solid alloy at a given pressure. In the following section these will be compared to experimental melting curves, including eutectic melting temperatures in binary systems, to show that the ΔS_m term can be reasonably estimated as R ln2 per mole atoms at high pressure conditions. This will serve as a basis for estimating multicomponent (ternary) phase diagrams relevant to Earth's core at 330 GPa.

Application to Experimental Melting Temperatures

Fischer [this volume] has summarized experimental constraints on the melting curve of Fe at high pressures, and also binary eutectic temperatures in various Fe-rich systems. In addition, melting curves are available for endmember compounds FeO [*Fischer and Campbell*, 2010], Fe_3C [*Lord et al.*, 2009], and FeSi [*Lord et al.*, 2010; *Fischer et al.*, 2013]. These melting temperatures can be applied to Equation (2) above to obtain estimates of ΔS_m or of solid–melt partitioning.

As an example, consider the Fe–FeO system. Available evidence from X-ray diffraction experiments indicates that there is very limited departure in the endmembers of this binary system from pure Fe and FeO, so the temperature along the two branches of the liquidus can be calculated from Equations (2) and (5) as

$$(6) \qquad T = \frac{T_m^{Fe}}{1 - \frac{R}{\Delta S_m^{Fe}} \ln\left(X_{Fe}^L\right)} \quad \text{and} \quad T = \frac{T_m^{FeO}}{1 - \frac{R}{\Delta S_m^{FeO}} \ln\left(4\, X_{Fe}^L X_O^L\right)}$$

where the left equation describes the liquidus on the Fe-rich side of the eutectic composition, and the right equation describes the liquidus on the FeO-rich side. At the eutectic both equations

describe the same temperature (T_{eut}), and the eutectic composition can be computed from this, using also $X_{Fe}^{L} + X_{O}^{L} = 1$. For comparison, at 80 GPa the melting points of Fe, FeO, and their eutectic are approximately 3500 K, 3200 K, and 2600 K respectively [*Anzellini et al.*, 2013; *Fischer and Campbell*, 2010; *Seagle et al.*, 2008; *Fischer*, this volume]. A pressure of 80 GPa is practical for this comparison because it is near the upper limit of experimentally-determined melting points for FeO and the eutectic, and it is a sufficiently pressure to be considered the 'high pressure' regime insofar as the entropy change upon melting is concerned. These experimental melting points can be reconciled with Equation (6) if the entropy change $\Delta S_m = 0.75\,R$ per mole of atoms for both Fe and FeO (Figure 1). This produces a eutectic composition at 80 GPa of 7.8 wt% oxygen, slightly lower than the ~10.5 wt% O reported by *Seagle et al*. [2008] but within 2σ uncertainties of those experiments.

In the high pressure limit, when $\Delta V_m \to 0$, the entropy change of melting for simple substances is expected to approach $\Delta S_m \to R \ln 2$ [*Stishov et al.*, 1973; *Stishov*, 1988]. More exactly [*Tallon*, 1980],

$$\Delta S_m = R\ln 2 + \alpha K_T \Delta V_m = R\ln 2 + \gamma C_V \frac{\Delta V_m}{V} \quad (7)$$

where $\gamma = \alpha K_T V / C_V$ is the Grüneisen parameter of the substance. Reasonable estimates for iron alloys in Earth's core might be $\gamma \approx 1.3$, $C_V \approx 5\,R$ (including an approximate electronic heat capacity at high T) [*Brown and McQueen*, 1986], and $\Delta V_m/V \approx 1.5\%$ [*Laio et al.*, 2000], producing $\Delta S_m \approx 0.79\,R$, close to the value of $0.75\,R$ obtained from analysis of the Fe–FeO system. Ab initio and molecular dynamic studies have produced higher values of $\Delta S_m = 0.86$ R to

1.05 R for Fe at 330 GPa [*Laio et al.*, 2000; *Alfè et al.*, 2002; *Zhang et al.*, 2015]. As *Zhang et al.* [2015] noted however, these methods also overestimate ΔS_m for Fe at 1 bar by a similar amount.

The Fe–Fe_3C provides another useful case to consider, because the melting temperatures in this system have also been determined experimentally [*Lord et al.*, 2009; *Anzellini et al.*, 2013]. In this case the analog to Equation (6) becomes

$$(8) \qquad T = \frac{T_m^{Fe}}{1 - \frac{R}{\Delta S_m^{Fe}} \ln\left(X_{Fe}^{L}\right)} \quad \text{and} \quad T = \frac{T_m^{Fe_3C}}{1 - \frac{R}{\Delta S_m^{Fe_3C}} \ln\left(\frac{256}{27} X_{Fe}^{L\ 3} X_C^{L}\right)}$$

Here again it has been assumed that the solid endmembers Fe and Fe_3C are effectively stoichiometric, although this is a less well justified assumption than in the Fe–FeO system, as solid iron can contain up to 2 wt% C at 1 bar, and probably to some degree at high pressures too. Nevertheless, this is a minor correction. Using melting points at 80 GPa of 3500 K, 2900 K, and 2800 K for Fe, Fe_3C, and their eutectic, respectively [*Lord et al.*, 2009; *Anzellini et al.*, 2013] one finds that Equation (8) is satisfied with $\Delta S_m = 0.71\,R$ per mole of atoms for both Fe and Fe_3C (Figure 1). Again this value is slightly greater than the high pressure limit of R ln2, indicating that a value of $\Delta S_m = 0.70\text{-}0.75\,R$ is a reasonable approximation with which to estimate the thermodynamics of melting at high pressures comparable to those in Earth's core.

An important difficulty in the Fe–C system is that at higher pressures the relevant carbide endmember is probably Fe_7C_3, not Fe_3C. Less is known about the physical properties of Fe_7C_3, but it is evident from the limited melting data on this phase by *Lord et al.* [2009] that its melting point is much higher than that of Fe_3C, perhaps 3500 K at 80 GPa. This strongly suggests that the

eutectic melting point depression in Fe–Fe_7C_3 is somewhat less than that of Fe–Fe_3C, but there are no experimental data yet to verify this. In this paper Fe_3C will be used as the relevant carbide phase, acknowledging that an important improvement will be to measure the iron-carbide eutectic at sufficiently high pressure (~120 GPa [*Lord et al.*, 2009]) that Fe_7C_3 is the solidus carbide phase.

The converse problem presently exists with the high pressure melting in the iron–sulfide system. Experimental measurements of Fe–Fe_3S eutectic melting have been accomplished up to 175 GPa [*Kamada et al.*, 2012], with remarkable consistency among results from different authors [*Campbell et al.*, 2007; *Chudinovskikh and Boehler*, 2007; *Stewart et al.*, 2007; *Morard et al.*, 2008; *Kamada et al.*, 2010; 2012]. However, the melting curve of the endmember Fe_3S has not been measured. Using ΔS_m = 0.70-0.75 R as above, and the reported melting point depression for the Fe–Fe_3S system at high pressures (1050 K from *Fischer* [this volume]), the melting point of Fe_3S can be estimated using an analysis similar to that in Equation (8):

$$(9) \qquad T = \frac{T_m^{Fe}}{1 - \frac{R}{\Delta S_m^{Fe}} \ln\left(X_{Fe}^{L}\right)} \quad \text{and} \quad T = \frac{T_m^{Fe_3S}}{1 - \frac{R}{\Delta S_m^{Fe_3S}} \ln\left(\frac{256}{27} X_{Fe}^{L\ 3} X_C^{L}\right)}$$

The resulting melting point at 80 GPa is ~2450 K (Figure 1). This is indistinguishable from T_{eut} and correspondingly places the eutectic composition near 16 wt% S, which is the sulfur content in Fe_3S. Although not impossible, this is higher than the eutectic composition of 12.5% S at 85 GPa reported by *Kamada et al.* [2012], and likely reflects some nonideality in the Fe–S system persisting to high pressure. Here we have assumed again that any deviation from ideal Fe_3S stoichiometry is negligible, although there is evidence that this is not strictly correct [*Li et al.*,

2001].

The Fe–Si binary system is even more challenging to treat, in the absence of Si partitioning measurements between solid and melt. Using again 80 GPa as an example condition to compare to experimental results, the subsolidus phase diagram shows eutectic melting between *fcc*-Fe and a *B2*-structured Si-rich alloy, although at pressures >90 GPa the Fe-rich phase becomes *hcp* [*Fischer et al.*, 2013; *Anzellini et al.*, 2013]. At 80 GPa the melting temperature of Fe is approximately 3500 K. There is extensive solid solution of Si into both the *fcc* and *hcp* structures of Fe, plus various intermetallics at low pressures, and also evidence for extensive solid solution in the *B2* phase of FeSi, perhaps to as low as ~25 mol% Si [*Fischer et al.*, 2013]. Consequently, analysis of this phase diagram is not as easily simplified as the Fe–FeO, Fe–Fe_3C, and Fe–Fe_3S systems above. Nonetheless, Equation (2) provides some insight into the Si partitioning behavior when the high-pressure melting behavior of Fe–Si alloys is considered. As summarized by *Fischer* [this volume], the melting point depression in Fe–Si alloys at high pressure is 200±200 K, which is a relatively small but uncertain degree. Using these values with ΔS_m = 0.70–0.75 R as before, Equation (2) yields solid-liquid partitioning of Fe between metal and melt of X_{Fe}^{S}/X_{Fe}^{L} = 1.00–1.10 at the eutectic temperature, consistent with the narrow *fcc*+melt phase loops at 80 GPa described by *Fischer et al.* [2013] on the basis of X-ray diffraction data. Additional constraints from future work will be required to obtain the compositions of the coexisting phases. Nevertheless, it is evident from this analysis that the partitioning of Si between solid metal and melt is weak, and not by itself likely to produce a large density contrast like the 7% change observed at the inner core boundary [*Masters and Gubbins*, 2003].

Phase Relations at Inner Core Boundary Conditions

A principal result from the previous section is that the available experimental data on high-pressure melting of Fe-rich alloys supports an estimate of ΔS_m = 0.70–0.75 R for their entropy of melting. This value of ΔS_m is slightly higher than the $\Delta V_m \rightarrow 0$ limit of R ln2 [*Stishov*, 1988], consistent with the observation that the Fe melting curve remains positive to core pressures and has a ΔV_m of 1–2% [*Laio et al.*, 2000; *Alfè et al.*, 2002]. The difference between 0.70 and 075 has an effect of only ~100 K in calculated melting temperatures, and going forward we will assume that ΔS_m = 0.75 R is a suitable estimate for any Fe-rich alloy composition. In this section, the analysis of melting phase relations will be extended to 330 GPa, the pressure at Earth's inner core boundary, to predict of the chemistry of melting in Fe-rich systems under conditions at which no such experimental data exist. The results will be speculative, as they are based on assumptions of ideal mixing and extrapolations of melting curves, but they can serve as a roadmap for future experimental exploration into these phase diagrams.

The melting curve of Fe has been extensively studied with static and dynamic experimental methods, as well as ab initio calculations, because of its key importance to the thermal structure of Earth's interior. Following *Fischer* [this volume], in this chapter the melting curve of *Anzellini et al.* [2013] will be used as a reference for pure Fe (i.e. 6200 K at 330 GPa), mainly for consistency as the experimental techniques used in that study (X-ray diffraction in a laser heated diamond anvil cell) were similar to those used in several studies of eutectic melting in Fe-binary systems (e.g. *Campbell et al.*, 2007; *Seagle et al.*, 2008; *Morard et al.*, 2008; *Asanuma et al.*, 2010; *Kamada et al.*, 2010, 2012; *Fischer et al.*, 2012; 2013). Likewise, for convenience the extrapolation of binary eutectic temperatures to the ICB pressure will follow the summary of

Fischer [this volume]. As *Fischer* [this volume] observed, the eutectic depressions in the Fe–FeO, Fe–Fe_3S, Fe–Fe_3C, and Fe–FeSi systems remain approximately constant, within experimental uncertainty, over the high-pressure ranges in which they have been investigated, and therefore their extrapolations to 330 GPa can simply track the *Anzellini et al.* [2013] melting curve of Fe. Constant eutectic depressions of 900 K (Fe–FeO), 700 K (Fe–Fe_3C), 1050 K (Fe–Fe_3S), and 200 K (Fe–FeSi) will be applied for the respective binary systems, and the thermodynamic framework of the previous section will be used to calculate phase relations at the inner core boundary.

As in the previous section, Equations (6), (8), and/or (9) can be used to calculate liquidus phase relations coexisting with solid phases Fe, FeO, Fe_3C, and Fe_3S. For now we can approximate these phases as pure, i.e. $a_i^S = 1$ in Equation (2) for each of these components. The phase diagrams produced here are restricted to the Fe–O–C–S system, because the known solid solution in Fe–Si alloys is so extensive that without further information it is pointless to project phase relations with an Fe–Si component to inner core conditions. It is also assumed that the relevant endmembers are FeO, Fe_3C, and Fe_3S, although it is known that Fe_7C_3 plays an important role at high pressures, and that Fe_3S dissociates to an unidentified sulfide at $P > 250$ GPa [*Ozawa et al.*, 2013].

For each ternary system, cotectic curves and eutectic points are obtained by simultaneous solution of Equations (6), (8), and/or (9), with the additional constraint $X_{Fe}+X_O+X_C+X_S=1$. The results are shown in Figure 2. In the 330 GPa ternary systems, the eutectic temperatures lie in the range 4600–4900 K, which are not unreasonable lower bounds on the ICB temperature. The

eutectic compositions in the Fe–O–S and Fe–C–S ternaries contain 10–12 wt% light element, which is consistent with that needed to explain the core density deficit, but the Fe–O–C eutectic is significantly more Fe-rich (5.5 wt% O+C), suggesting that sulfur may be important to the solid/melt phase relations to obtain a core composition that is consistent with the geophysical constraint that the liquid is ~7% less dense than the coexisting solid [*Masters and Gubbins*, 2003]. The same analysis can be applied to the Fe–O–C–S quaternary system, from which one obtains a eutectic temperature T_{eut} = 4290 K at X_O = 0.08, X_C = 0.07, X_S = 0.13. These multicomponent eutectic compositions are compatible with the 7% density contrast observed at the inner core boundary.

The binary eutectic melting point depressions, adapted here from *Fischer* [this volume], are critical input to the calculated phase diagrams in Figure 2, and uncertainty in these melting points propagate significantly to the liquidus phase boundary compositions. To give an example, increasing the Fe–O eutectic depression from ΔT_{eut} = 900 K to ΔT_{eut} = 1200 K would shift the calculated Fe–O eutectic composition at 330 GPa from X_O = 0.08 to X_O = 0.12, with corresponding shift in the neighboring cotectic curves illustrated in Figure 2. *Komabayashi* [2014] obtains a much greater oxygen content in the 330 GPa Fe-O eutectic (9 wt%) by invoking ΔT_{eut} = 2000 K, which is not supported by experiments at lower pressures [*Seagle et al.*, 2008; *Fischer*, this volume]. This example underscores the importance of obtaining greater experimental constraints on the melting curves of Fe-alloys at pressures approaching those of Earth's inner core boundary.

There are very few multicomponent data at sufficiently high pressure with which to compare

such calculations, but *Terasaki et al.* [2011] report Fe–O–S eutectic melting temperatures that are indistinguishable from the Fe–S binary eutectic [*Kamada et* al., 2012] up to 140 GPa. This result does not match well the analysis presented here (~500 K difference between the Fe–O–S and Fe–S eutectics), and further highlights the need for more experimental investigations to provide a larger foundation upon which thermodynamic models of candidate core-forming alloys can be improved.

Outlook

The calculated phase diagrams in Figure 2 serve as examples of how reasonable approximations (an ideal associated solution model; an entropy change of melting for all alloys $\Delta S_m = 0.75\,R$, slightly above the $\Delta V_m \rightarrow 0$ limit; binary eutectic melting point depression unchanging with pressure) allow the construction of useful Fe–X liquidus diagrams using only melting curves as experimental input. Obviously this approach has limitations, but these can be overcome with continued effort from both experimental and ab initio methods. Of primary importance will be solid/liquid partitioning experiments at the ICB pressure, 330 GPa. These are essential to understand Fe-Si or other systems in which significant solid solution exists. Experiments like these have not yet been reported, but continuing advances both in high pressure generation [e.g. *Tateno et al.*, 2010; *Dubrovinsky et al.*, 2012] and petrological examination of recovered diamond anvil samples [e.g. *Seibert et al.*, 2012; *Nomura et al.*, 2013; *Ozawa et al.*, 2013] indicate that they are on the horizon. Even a relatively small number of phase equilibria experiments would allow important refinement of the calculated phase diagrams in Figure 2, and subsolidus experiments can also provide useful constraints on the extent of solid solution expected in metal coexisting with melt. Additionally, extending the melting curves to higher

pressures will allow more accurate phase diagram calculations from the data. Not only eutectic melting but also endmember melting curves are useful input to a thermodynamic framework in which the chemistry of the inner core boundary can be understood.

References

Alfè D., Price G. D., and Gillan M. J. (2002) Iron under Earth's core conditions: Liquid-state thermodynamics and high-pressure melting curve from ab initio calculations. *Phys. Rev. B*, 65, 165118.

Alfè D., Gillan M. J., and Price G. D. (2007) Temperature and composition of the Earth's core. *Contemp. Phys.*, 48, 63-80.

Antonangeli D., Siebert J., Badro J., Farber D. L., Fiquet G., Morard G., and Ryerson F. J. (2010) Composition of the Earth's inner core from high-pressure sound velocity measurements in Fe–Ni–Si alloys. *Earth Planet. Sci. Lett.*, 295, 292-296.

Anzellini S., Dewaele A., Mezouar M., Loubeyre P., and Morard G. (2013) Melting of iron at Earth's inner core boundary based on fast X-ray diffraction. *Science*, 340, 464-466.

Asanuma H., Ohtani E., Sakai T., Terasaki H., Kamada S., Kondo T., and Kikegawa T. (2010) Melting of iron–silicon alloy up to the core–mantle boundary pressure: implications to the thermal structure of the Earth's core. *Phys. Chem. Minerals*, 37, 353-359.

Badro J., Fiquet G., Guyot F., Gregoryanz E., Occelli F., Antonangeli D., d'Astuto M. (2007) Effect of light elements on the sound velocities in solid iron: Implications for the composition of Earth's core. *Earth Planet. Sci. Lett.*, 254, 233–238.

Birch F. (1952) Elasticity and composition of earth's interior. *J. Geophys. Res.* 57, 227-286.

Brown J. M., Ahrens T. J., and Shampine D. L. (1984) Hugoniot data for pyrrhotite and the Earth's core. *J. Geophys. Res.*, 89, 6041-6048.

Brown J. M. and McQueen R. G. (1986) Phase transitions, Grüneisen parameter, and elasticity for shocked iron between 77 GPa and 400 GPa. *J. Geophys. Res.*, 91, 7485-7494.

Campbell A. J., Seagle C. S., Heinz D. L., Shen G., and Prakapenka V. B. (2007) Partial melting in the iron-sulfur system at high pressure: A synchrotron X-ray diffraction study. *Phys. Earth Planet. Int.*, 162, 119-128.

Campbell A. J., Danielson L., Righter K., Seagle C. T., Wang Y., and Prakapenka V. B. (2009) High pressure effects on the iron-iron oxide and nickel-nickel oxide oxygen fugacity buffers. *Earth Planet. Sci. Lett.*, 286, 556-564.

Chen B., Li Z., Zhang D., Liu J., Hu M. Y., Zhao J., Bi W., Alp E. E., Xiao Y., Chow P., and Li J. (2014) Hidden carbon in Earth's inner core revealed by shear softening in dense Fe_7C_3. *Proc. Nat. Acad. Sci.*, 111, 17755-17758.

Chuang Y.-Y. and Chang Y. A. (1982) Extension of the associated solution model to ternary metal-sulfur melts: Cu-Ni-S. *Metall. Trans. B*, 13, 379-385.

Chudinovskikh L. and Boehler R. (2007) Eutectic melting in the system Fe-S to 44 GPa. *Earth Planet. Sci. Lett.*, 257, 97-103.

Dewaele A., Loubeyre P., Occelli F., Mezouar M., Dorogokupets P. I., and Torrent M. (2006) Quasihydrostatic equation of state of iron above 2 Mbar. *Phys. Rev. Lett.*, 97, 215504.

Dubrovinsky L., Dubrovinskaia N., Prakapenka V. B., and Abakumov A. (2012) Implementation of micro-ball nanodiamond anvils for high-pressure studies above 6 Mbar. *Nature Comm.*, 3, 1163.

Dziewonski A. M. and Anderson D. L. (1981) Preliminary reference Earth model. *Phys. Earth Planet. Inter.*, 25, 297-356.

Fei Y., Li J., Bartka C. M. and Prewitt C. T. (2000) Structure type and bulk modulus of Fe_3S, a new iron-sulfur compound. *Am. Mineral*., 85, 1830-1833.

Fischer R. A. and Campbell A. J. (2010) High pressure melting of wüstite. *Am. Mineral.*, 95, 1473-1477.

Fischer R. A., Campbell A. J., Shofner G. A., Lord O. T., Dera P., and Prakapenka V. B. (2011) Equation of state and phase diagram of FeO. *Earth Planet. Sci. Lett.*, 304, 496-502.

Fischer R. A., Campbell A. J., Caracas R., Reaman D. M., Dera P., and Prakapenka V. B. (2012) Equation of state and phase diagram of Fe–16Si alloy as a candidate component of Earth's core. *Earth Planet. Sci. Lett.*, 357-358, 268-276.

Fischer R. A., Campbell A. J., Reaman D. M., Miller N. A., Heinz D. L., Dera P., and Prakapenka V. B. (2013) Phase diagrams in the Fe–FeSi system at high pressures and temperatures. *Earth Planet. Sci. Lett.*, 373, 54-64.

Fischer R. A., Campbell A. J., Caracas R., Reaman D. M., Heinz D. L., Dera P., and Prakapenka V. B. (2014) Equations of state in the Fe–FeSi system at high pressures and temperatures. *J.*

Geophys. Res., 119, 2810-2827.

Ghiorso M. S. (2004) An equation of state for silicate melts. I. Formulation of a general model. *Am. J. Sci.*, 304, 637-678.

Jeanloz R. and Ahrens T. J. (1980) Equations of state of FeO and CaO. *Geophys. J. R. Astr. Soc.*, 62, 505-528.

Kamada S., Terasaki H., Ohtani E., Sakai T., Kikegawa T., Ohishi Y., Hirao N., Sata N., and Kondo T. (2010) Phase relationships of the Fe–FeS system in conditions up to the Earth's outer core. *Earth Planet. Sci. Lett.*, 294, 94–100.

Kamada S., Ohtani E., Terasaki H., Sakai T., Miyahara M., Ohishi Y., and Hirao N. (2012) Melting relationships in the Fe–Fe_3S system up to the outer core conditions. *Earth Planet. Sci. Lett.* 359-360, 26-33.

Kamada S., Ohtani E., Fukui H., Sakai T., Terasaki H., Takahashi S., Shibazaki Y., Tsutsui S., Baron A. Q. R., Hirao N., and Ohishi Y. (2014a) The sound velocity measurements of Fe_3S. *Am. Mineral.*, 99, 98-101.

Kamada S., Ohtani E., Terasaki H., Sakai T., Takahashi S., Hirao N. and Ohishi Y. (2014b) Equation of state of Fe3S at room temperature up to 2 megabars. *Phys. Earth Planet. Int.*, 228, 106-113.

Komabayashi T. (2014) Thermodynamics of melting relations in the system Fe-FeO at high pressure: Implications for oxygen in the Earth's core. *J. Geophys. Res.*, 119,

doi:10.1002/2014JB010980.

Laio A., Bernard S., Chiarotti G. L., Scandolo S., and Tosatti E. (2000) Physics of iron at Earth's core conditions. *Science*, 287, 1027-1030.

Li J., Fei Y., Mao H. K., Hirose K., and Shieh S. R. (2001) Sulfur in the Earth's inner core. *Earth Planet. Sci. Lett.* 193, 509-514.

Litasov K. D., Sharygin I. S., Dorogokupets P. I., Shatskiy A., Gavryushkin P. N., Sokolova T. S., Ohtani E., Li J., and Funakoshi K. (2013) Thermal equation of state and thermodynamic properties of iron carbide Fe_3C to 31 GPa and 1473 K. *J. Geophys. Res.*, 118, 1-11, doi: 10.1002/2013JB010270.

Lord O. T., Walter M. J., Dasgupta R., Walker D., and Clark S. M. (2009) Melting in the Fe–C system to 70 GPa. *Earth Planet. Sci. Lett.*, 284, 157-167.

Lord O. T., Walter M. J., Dobson D. P., Armstrong L., Clark S. M., Kleppe A. (2010) The FeSi phase diagram to 150 GPa. *J. Geophys. Res*., 115, B06208.

Mao Z., Lin J.-F., Liu J., Alatas A., Gao L., Zhao J., and Mao H.-K. (2012) Sound velocities of Fe and Fe-Si alloy in the Earth's core. *Proc. Nat. Acad. Sci.*, 109, 10239–10244.

Masters G. and Gubbins D. (2003) On the resolution of density within the Earth. *Phys. Earth Planet. Int.*, 140, 159-167.

McDonough, W. F. (2003) Compositional model for the Earth's core. In: *Treatise of*

Geochemistry, Vol. 2, ed. Carlson R. W., pp. 547-568. Elsevier Ltd.

Morard G., Andrault D., Guignot N., Sanloup C., Mezouar M., Petitgirard S., and Fiquet G. (2008) In situ determination of Fe–Fe_3S phase diagram and liquid structural properties up to 65 GPa. *Earth Planet. Sci. Lett.* 272, 620-626.

Morard G., Siebert J., Andrault D., Guignot N., Garbarino G., Guyot F. J., and Antonangeli D. (2013) The Earth's core composition from high pressure density measurements of liquid iron alloys. *Earth Planet. Sci. Lett.*, 373, 169-178.

Nomura R., Hirose K., Uesugi K., Ohishi Y., Tsuchiyama A., Miyake A., and Ueno Y. (2014) Low core–mantle boundary temperature inferred from the solidus of pyrolite. *Science*, 343, 52-525.

Ozawa H., Hirose K., Suzuki T., Ohishi Y., and Hirao N. (2013) Decomposition of Fe_3S above 250 GPa. *Geophys. Res. Lett.*, 40, 4845-4849.

Prigogine I. and Defay R. (1954) *Chemical Thermodynamics*. Longmans Green, London, 500 pp.

Sata N., Hirose K., Shen G., Nakajima Y., Ohishi Y., and Hirao N. (2010) Compression of FeSi, Fe_3C, $Fe_{0.95}O$, and FeS under the core pressures and implication for light element in the Earth's core. *J. Geophys. Res.*, 115, B09204, doi:10.1029/2009jb006975.

Seagle C. T., Campbell A. J., Heinz D. L., Shen G. and Prakapenka V. B. (2006) Thermal equation of state of Fe_3S and implications for sulfur in Earth's core. *J. Geophys. Res.* 111, B06209.

Seagle C. S., Heinz D. L., Campbell A. J., Prakapenka V. B., and Wanless S. T. (2008) Melting and thermal expansion in the Fe – FeO system at high pressure. *Earth Planet. Sci. Lett.*, 265, 655-665.

Sharma R. C. and Chang Y. A. (1979) Thermodynamics and phase relationships of transition metal-sulfur systems: Part III. Thermodynamics properties of the Fe-S liquid phase and calculation of the Fe-S phase diagram. *Metall. Trans. B*, 10, 103-108.

Stevenson D. J. (1981) Models of the Earth's core. *Science*, 214, 611-619.

Stewart A. J., Schmidt M. W., van Westrenen W., and Liebske C. (2007) Mars: A new core-crystallization regime. *Science*, 316, 1323-1325.

Stishov S. M. (1988) Entropy, disorder, melting. *Sov. Phys. Usp.*, 31, 52–67.

Stishov S. M., Makarenko I. N., Ivanov V. A., and Nikolaenko A. M. (1973) On the entropy of melting. *Phys. Lett. A*, 45, 18.

Svendsen B., Anderson W. W., Ahrens T. J., and Bass J. D. (1989) Ideal Fe–FeS, Fe–FeO phase relations and Earth's core. *Phys. Earth Planet. Int.*, 55, 154-186.

Tallon J. L. (1980) The entropy change on melting of simple substances. *Phys. Lett.*, 76A, 139-142.

Tateno S., Hirose K., Ohishi Y., and Tatsumi Y. (2010) The structure of iron in Earth's inner core. *Science*, 330, 359-361.

Terasaki H., Kamada S., Sakai T., Ohtani E., Hirao N. and Ohishi Y. (2011) Liquidus and solidus temperatures of a Fe–O–S alloy up to the pressures of the outer core: Implications for the thermal structure of Earth's core. *Earth Plan. Sci. Lett.*, 304, 559-564.

Wen S. and Nekvasil H. (1994) Ideal associated solutions: Application to the system albite–quartz–H_2O. *Am. Mineral.*, 79, 316-331.

Williams Q. and Jeanloz R. (1990) Melting relations in the iron–sulfur system at ultra-high pressures: Implications for the thermal state of the Earth. *J. Geophys. Res.*, 95, 19299.

Zhang W.-J., Liu Z.-Y., Liu Z.-L. and Cai L.-C. (2015) Melting curves and entropy of melting of iron under Earth's core conditions. *Phys. Earth Planet. Int.*, 244, 69-77.

Zhang Y. and Yin Q.-Z. (2012) Carbon and other light element contents in the Earth's core based on first-principles molecular dynamics. *Proc. Nat. Acad. Sci.*, 109, 19579-19583.

Figure Captions

Figure 1. Binary phase diagrams for Fe–FeO, Fe–Fe_3C, and Fe–Fe_3S at 80 GPa, calculated from experimental melting temperatures and Equations (6), (8), and (9). Black ovals: *Anzellini et al. 2013*; dark gray oval: *Seagle et al., 2009*; light gray oval: *Fischer and Campbell, 2009*; hatched ovals: *Lord et al., 2009*; white oval: *Kamada et al., 2012*.

Figure 2. Ternary phase diagrams of Fe-rich alloys at 330 GPa, calculated from experimental melting temperatures extrapolated to inner core boundary conditions. Binary and ternary eutectic compositions (mole fractions) and temperatures are labeled. The melting temperature of Fe is 6200 K [*Anzellini et al.*, 2013], and those of FeO (8370 K), Fe_3C (6310 K), and Fe_3S (5460 K) were calculated from Equations (6), (8), and (9) as described in the text, using eutectic melting point depressions summarized by *Fischer* [this volume] and a value of $\Delta S_m = 0.75\,R$ per mole atoms. a) Fe-FeO-Fe_3C ternary. b) Fe-FeO-Fe_3S ternary. c) Fe-Fe_3C-Fe_3S ternary.

Figure 1

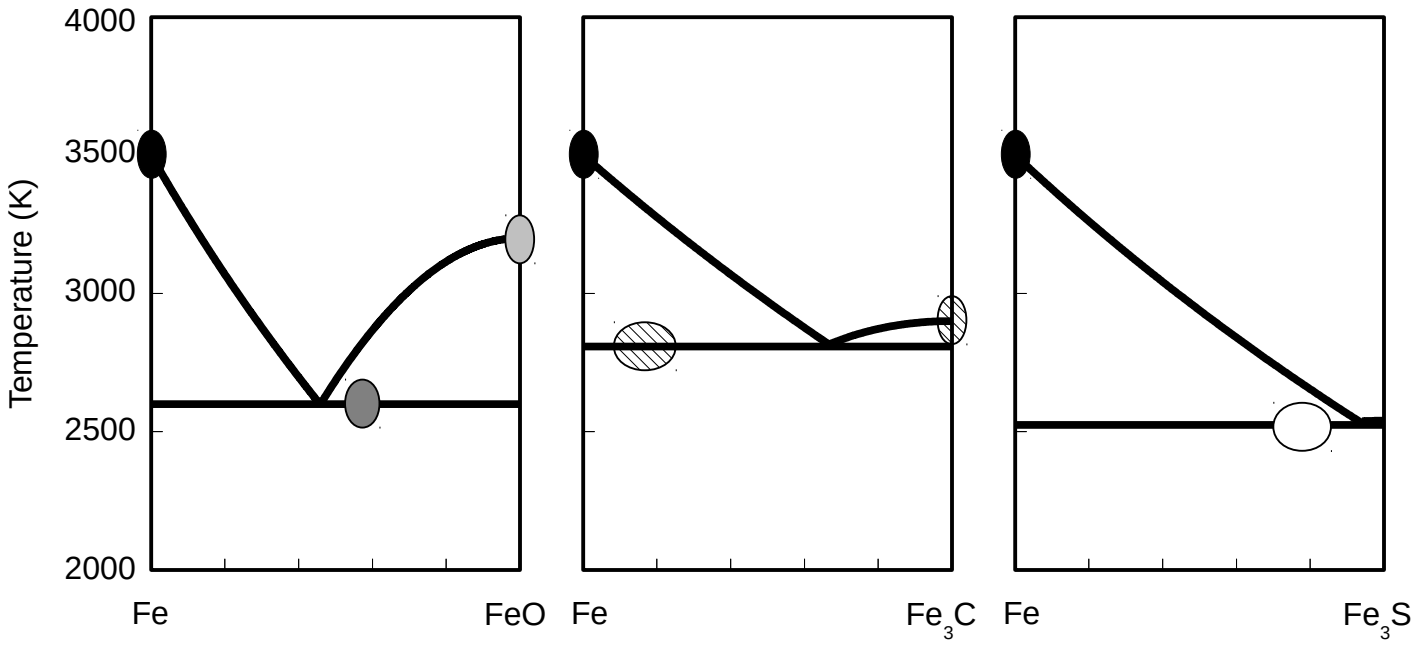

Figure 2 a)

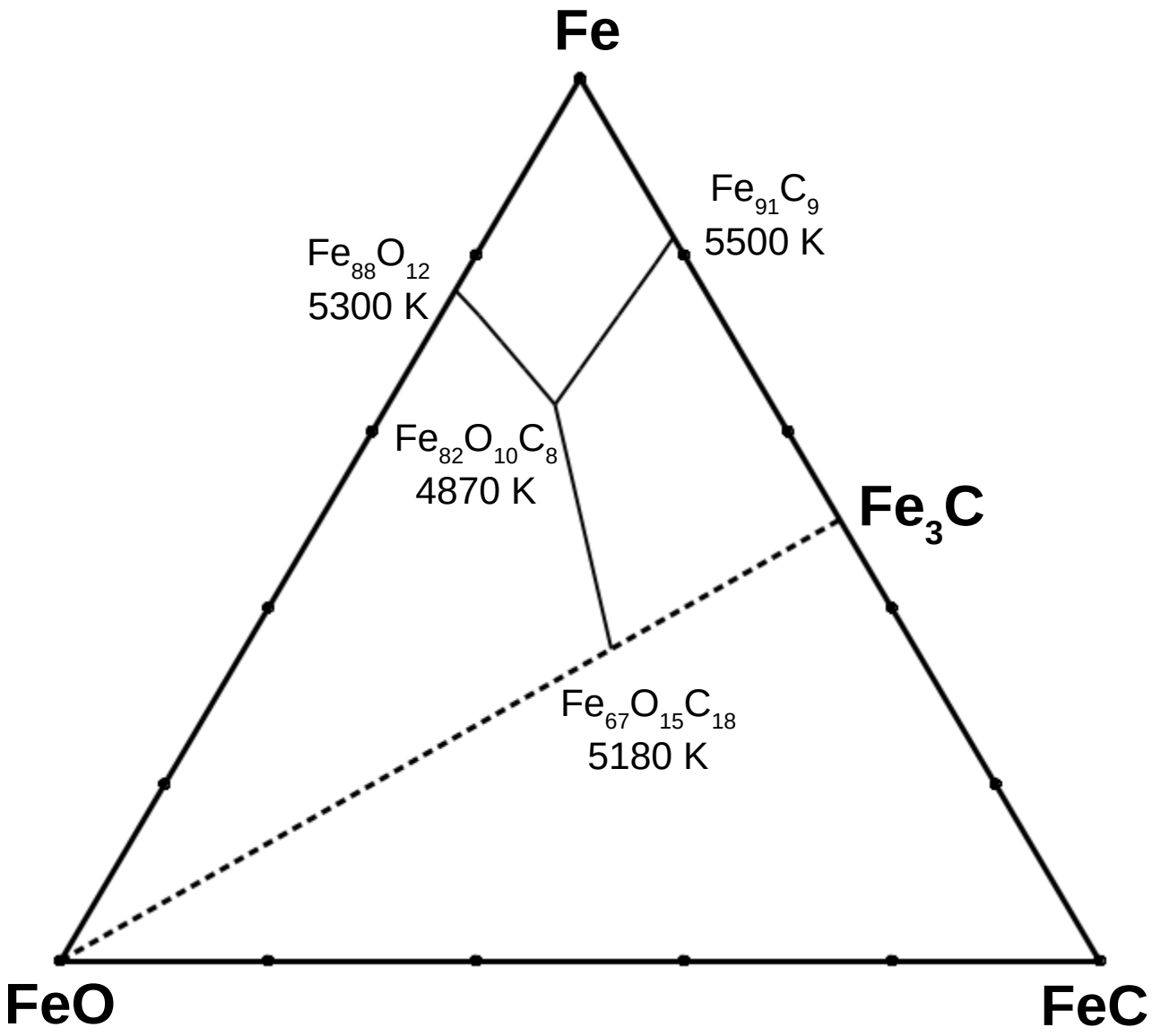
Fe
Fe91C9
5500 K
Fe88O12
5300 K
Fe82O10C8
4870 K
Fe3C
Fe67O15C18
5180 K
FeO
FeC

Figure 2 b)

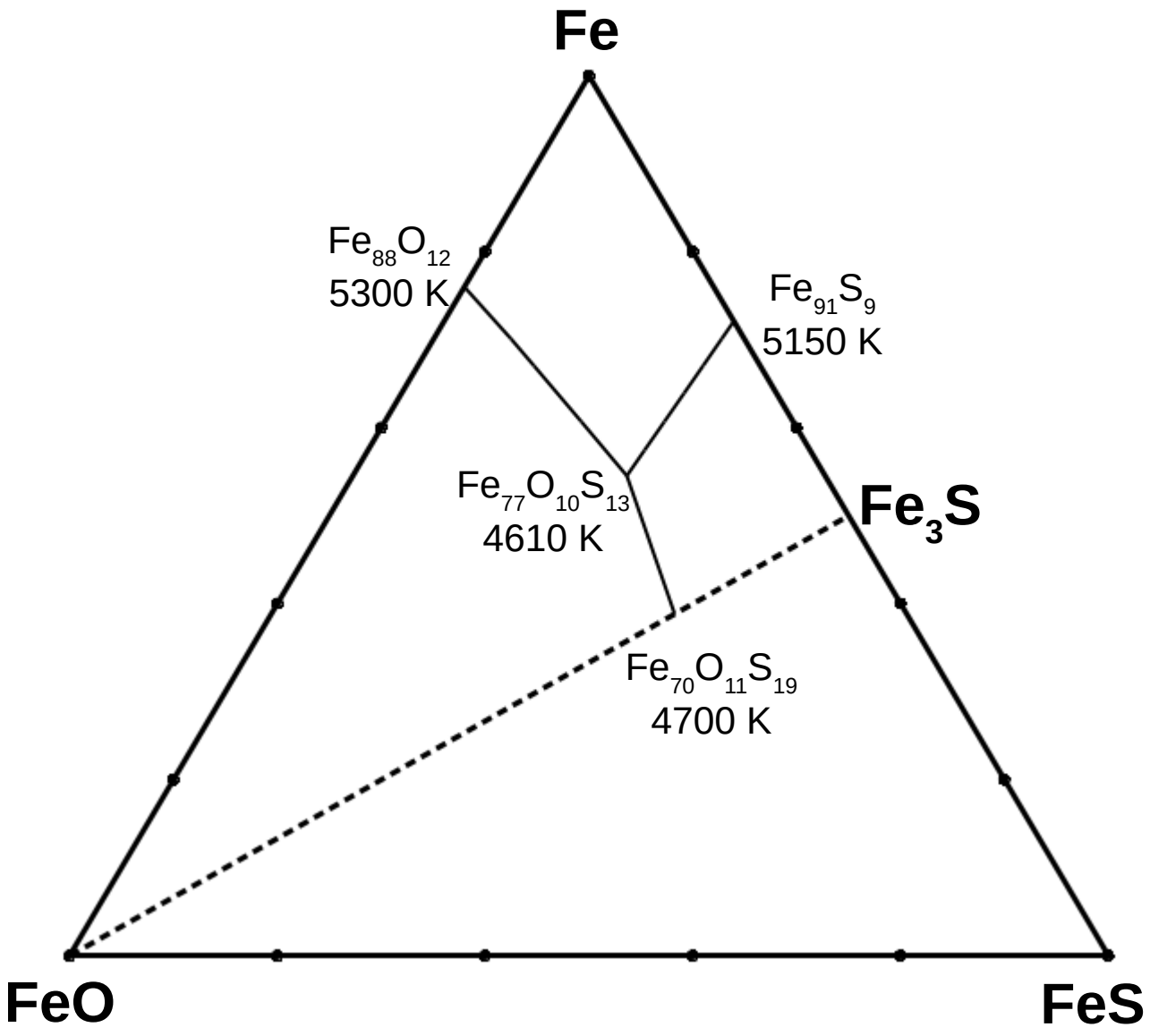
Fe
Fe88O12
5300 K
Fe91S9
5150 K
Fe77O10S13
4610 K
Fe3S
Fe70O11S19
4700 K
FeO
FeS

Figure 2 c)

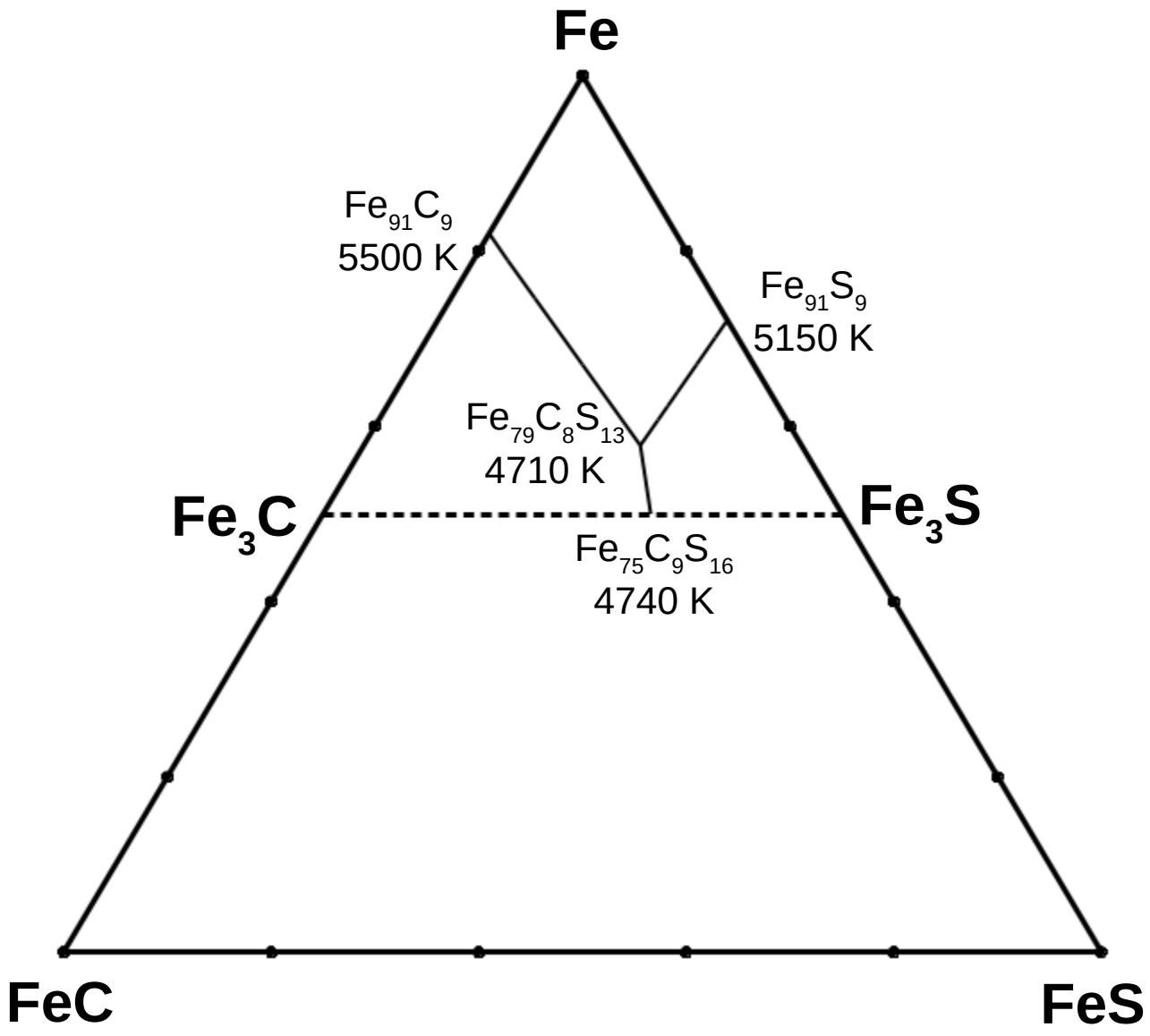
Fe
Fe91C9
5500 K
Fe91S9
5150 K
Fe79C8S13
4710 K
Fe3C
Fe3S
Fe75C9S16
4740 K
FeC
FeS